



An eco-friendly method for synthesis of Cu₂O/rGO/PANI composite using *Citrus maxima* juice for supercapacitor application

Sadhna Rai¹, Rabina Bhujel¹, Joydeep Biswas², and Bibhu P. Swain^{3,*}

¹Centre for Materials Science and Nanotechnology, Sikkim Manipal Institute of Technology, Sikkim Manipal University, East Sikkim, Majhitar 737136, India

²Department of Chemistry, Sikkim Manipal Institute of Technology, Sikkim Manipal University, East Sikkim, Majhitar 737136, India

³Department of Physics, National Institute of Technology, Manipur, Langol, Manipur 795004, India

Received: 14 April 2021

Accepted: 4 October 2021

Published online:
12 October 2021

© The Author(s), under exclusive licence to Springer Science+Business Media, LLC, part of Springer Nature 2021

ABSTRACT

An inexpensive and eco-friendly method has been reported for the straightforward synthesis of cuprous oxide/reduced graphene oxide/polyaniline (Cu₂O/rGO/PANI) composite. *Citrus maxima* (Pomelo) juice was used as a reducing agent to synthesize Cu₂O/rGO composite, and further polyaniline was grown on it. The Fourier-transform infrared, UV–visible, and Raman spectroscopy results suggested that Cu₂O/rGO/PANI composite was synthesized. X-ray diffraction patterns further suggested the synthesis of Cu₂O/rGO/PANI composite. The SEM results showed spherical Cu₂O particles decorated on rGO/PANI matrix. The composite was coated on a glassy carbon electrode and was used for electrochemical studies viz cyclic voltammetry, galvanostatic charge–discharge, and electrochemical impedance spectroscopy. The composite exhibited a high specific capacitance value of 496.61 F/g at a scan rate of 1 mV/s and showed excellent cycling stability.

1 Introduction

At present, the popularity of electronic gadgets in various sectors viz. industries, sports, medical, and offices have led to increased demand for energy. Currently, batteries are widely used in these gadgets due to their high energy density. However, they have the limitation of slow charging and a short life span. These limitations can be overcome by supercapacitors (SCs)

because they can be charged at a high-speed rate and possess a long lifetime [1]. Therefore, the researchers have devoted their energy and time to developing high-performance supercapacitors.

Various transition metal oxides (MOs) [2, 3], carbon materials [4], and conducting polymers (CPs) [5, 6] have been studied as electrode materials for SCs. When viewed individually, these materials have their benefits and drawbacks. Metal oxides and polymers undergo Faradaic reactions and are used as

Address correspondence to E-mail: bibhuprasad.swain@gmail.com; bpswain@nitmanipur.ac.in

electrodes for SCs. Copper oxide (CuO or Cu₂O) has been used as an electrode material for supercapacitor application due to its low cost and ability to give a high specific capacitance value (C_{sp}) [7–9]. However, they have low electronic conductivity, mechanical strength, and are chemically unstable. So, their application in flexible SCs is limited [10, 11]. Similarly, the CPs such as polyaniline (PANI) though they exhibit high C_{sp} value, becomes unstable during the cycling process. They undergo swelling, cracking, shrinking, and breaking, which adversely affects their properties [12]. The limitations of the MOs and CPs can be overcome by integrating a trendy carbon material of recent time, *i.e.*, graphene. Graphene is a versatile material with extraordinary conductivity, strength, flexibility, chemical stability, and surface area [13, 14]. Nevertheless, the synthesis of pristine graphene requires sophisticated instruments, and the yield is also low. This leads to an increase in its price. This problem is solved by synthesizing reduced graphene oxide (rGO) using a chemical synthesis process. It is a simple and economical process for the large-scale production of graphene. Recently, plant extracts have been used widely to synthesize rGO to eliminate the toxic chemicals involved in the chemical synthesis of rGO [15–18]. Moreover, the rGO synthesized using plant extracts are agglomerated and have a low specific area. This limits its use in supercapacitor applications. This problem can be tackled by adding MOs or CPs to rGO. They act as spacers and reduce agglomeration. Thus, we see that when integrated, these materials help in overcoming the drawbacks of their counterparts.

In recent years, researchers have numerous studies on MO–rGO–PANI composites for supercapacitor applications. Haldar et al. incorporated graphene in the Mn₃O₄/PANI matrix to make a supercapacitor electrode with a C_{sp} value of 1240 F/g at 2 A/g current density. This electrode showed stability of 96% even after 3000 cycles [19]. Zhu et al. assembled a CuO/rGO/PANI hybrid electrode to give a high C_{sp} value of 634.4 F/g at 1 A/g current density. This electrode was highly stable as it demonstrated 97.4% C_{sp} retention after 10,000 cycles [20]. Gupta et al. fabricated a flexible supercapacitor with PANI/rGO/Fe₂O₃ nanocomposite hydrogel coated on carbon cloth. The device exhibited an excellent C_{sp} value of 1124 Fg⁻¹ in 1 M H₂SO₄ at 0.25 Ag⁻¹ current density with charge retention of 82.2% [21]. Sinha et al. synthesized polyaniline/rGO/Ag₂O using a chemical

route and obtained a C_{sp} value of 897.9 F/g at a scan rate of 5 mV/s with excellent cycling stability of 87.1% after 5000 cycles [22]. Though the previous works showed excellent C_{sp} values with excellent charge retention, they used hydrazine (N₂H₄) to synthesize their material. N₂H₄ is highly toxic to human health as well as to the environment. Thus, in an attempt to eradicate the hazards of toxic chemicals, we present an environment-friendly procedure for the synthesis of Cu₂O/rGO/PANI (CRP) and its application as a supercapacitor electrode. Instead of the toxic chemical, we use *Citrus maxima* juice.

Citrus maxima, commonly known as pomelo, is a perennial plant which gives edible fruits. It grows in tropical and subtropical regions. In India, it is widely found in the northeastern and southern states. It has anti-inflammatory, anti-bacterial, anti-diabetic, and anti-carcinogenic properties [23]. The juice contains vitamin C, antioxidants such as beta-carotene, terpenoids, alkaloids, beta-sitosterol, carotene, polyphenols, and flavonoids. Flavonoids commonly neohesperidin, hesperidin, naringenin, naringin, and rutin are present in pomelo juice [24, 25]. These phytochemicals show reducing properties [26] which motivated the authors to synthesize CRP composites.

In this study, *Citrus maxima* juice has been employed for the synthesis of CRP composites. The successful synthesis of the composite was confirmed using various characterization techniques like XRD, FTIR, UV–Vis, Raman, and XPS. The as-synthesized composites were coated on glassy carbon electrodes and studied as electrode material for supercapacitors. The highest C_{sp} value of 496.61 F/g and excellent cycling stability of 88.49% was observed. The use of a bio-reducing agent contributes to the search for an eco-friendly and efficient reducing agent. This study shows that the CRP composite has a great potential application in supercapacitors.

2 Experimental

2.1 Chemical reagents

All the chemicals used for the synthesis process in the present study were of analytical grade, namely graphite fine powder (Loba Chemie Pvt. Ltd), sodium nitrate (NaNO₃) (Rankem), hydrogen peroxide (H₂O₂, 30%, Rankem), sulfuric acid (H₂SO₄, Rankem), copper sulfate pentahydrate (CuSO₄·5H₂O, Rankem)

and potassium permanganate (KMnO_4 , Rankem), hydrochloric acid (HCl, SD Fines Chem Ltd), aniline (SD Fines Chem Ltd), and ammonium persulfate (APS, Rankem). All solutions were made using deionized (DI) water.

2.2 Synthesis

Pomelo was washed and peeled. The juice was extracted by squeezing the pulp. It was then stored in the refrigerator for further use. Firstly, GO was synthesized using the modified Hummer's method as reported by Marcano *et al.* [27] A dispersion of 0.1 g GO and 0.06 M CuSO_4 in 50 mL DI water was made by magnetic stirring for 1 h. 0.5 mL aniline was added to the dispersion and stirred for 30 min. A solution was made by adding 0.2 g APS in 10 mL 1 M H_2SO_4 . This solution was added to the previous dispersion and was stirred in an ice bath for 5 h. Lastly, 40 mL of pomelo juice was added, and the mixture was refluxed at 90 °C for 6 h. The product was filtered using Whatman filter paper. It was washed with DI water and ethanol until a clear filtrate was obtained. It was dried and was coded CRP0.5. Two more such samples were made by varying the amount of aniline to 1 (CRP1) and 1.5 (CRP1.5) mL. Also, rGO was synthesized following the same procedure by excluding the addition of CuSO_4 , APS, and aniline. Similarly, PANI was synthesized by excluding the addition of GO, CuSO_4 , and pomelo juice.

2.3 Characterizations

The bondings and vibrations present in the CRP composites were studied using attenuated total reflection Fourier-transform infra-red (ATR-FTIR) spectroscopy recorded in IR Affinity-1S Shimadzu ATR-FTIR spectrometer using high-energy ceramic light as the IR source. The structures of CRP composites were analyzed by X-ray diffraction (XRD) recorded on Bruker D8 Advance X-ray diffractometer with Cu $\text{K}\alpha$ radiation ($\lambda = 0.154$ nm). The voltage, current, step size, and scan rate were 40 V, 25 mA, 0.02° , and $0.1^\circ/\text{s}$, respectively. The Raman data were acquired from an HR800-UV confocal micro-Raman spectrometer (Horiba JobinYvon, France made) using a laser source with an excitation wavelength of 532 nm. The optical properties were studied using UV-Visible spectroscopy. The UV-Vis

spectra were obtained from UV-1800 Shimadzu UV spectrophotometer. For the morphological study, scanning electron microscopy (SEM) images were taken from EVO MA18. X-ray photoelectron spectroscopy (XPS) spectra were recorded in PHI 5000 Versa Probe III with monochromatized Al K α -radiation (1486.6 eV).

2.4 Electrochemical studies

The electrochemical measurements were carried out in an electrochemical analyzer (CHI-608E). Cyclic voltammetry (CV), galvanostatic charge-discharge (GCD), and electrochemical impedance spectroscopy (EIS) were studied. The electrodes used were glassy carbon electrode (working electrode), Ag/AgCl (reference electrode), and platinum wire (counter electrode). An aqueous solution of 1 M H_2SO_4 was used as the electrolyte.

3 Results and discussion

3.1 Bonding and vibrations

To analyze the functional groups present in CRP composite, ATR-FTIR spectra (Fig. S1) were obtained. The spectrum of GO shows five prominent peaks located at 3303.8, 1733.9, 1602.7, 1171.8, and 1030.8 cm^{-1} corresponding to OH (alcohol) [28], C=O (carbonyl) [29], C=C (aromatic ring) [30], C-OH (carbon hydroxyl), and C-O (alkoxy) groups [31], respectively. In the spectrum of rGO, the peak for OH disappeared, suggesting the reduction of GO. It also possesses peaks located at 1522.8, 1281.8, and 1030.8 cm^{-1} attributed to C=C stretching of the aromatic ring [32], stretching vibrations of C-O of epoxy and alkoxy groups, respectively [29]. Further, the peaks at 761.6 and 667.9 cm^{-1} are for bending vibrations outside the C-H plane [33]. The previous peaks are also present in the spectrum of PANI with additional peaks at 1305.9 cm^{-1} , which is attributed to the C-N bending of the benzenoid ring [34]. However, in the spectra of CRP, one more peak is found. This peak at 1609.32 cm^{-1} corresponds to C=N stretching vibrations of the quinoid ring [35, 36]. The peak that appears at 504.3 cm^{-1} is for Cu-O stretching vibrations [37]. An additional peak appearing in all the spectra at 2367.4 cm^{-1} is for atmospheric CO_2 . From the FTIR analysis, it is

concluded that GO is reduced to some extent as the peaks for carbonyl, epoxy, and alkoxy groups still appear in the spectra of both rGO and CRP. Also, the presence of peaks for Cu–O and N–H suggest that Cu₂O/rGO/PANI is synthesized.

3.2 Structural analysis

In the diffraction pattern of GO, a peak at 11.05° corresponding to the (001) plane was found (Fig. 1a). After reducing with pomelo juice, a peak shift was observed with the appearance of a broad peak at 23.7°, which is caused by a disorder in the graphene sheets [38].

The pure PANI diffraction pattern (Fig. 1a) illustrates three peaks, an intense peak at 25.3° and two other peaks with lower intensities at 20.4° and 15.3° corresponding to (200), (020), and (011) planes of PANI, respectively [34]. The XRD pattern of CRP shows almost similar peaks to that of PANI (Fig. 1b). The peak for rGO is overlapped by PANI peaks, suggesting the inclusion of rGO in PANI. Further, they are also accompanied by diffraction peaks at 36.4, 42.3, 61.3, and 73.4°, corresponding to (111), (200), (220), and (311) planes of Cu₂O, respectively [39, 40]. XRD analysis thus confirms the synthesis of CRP composites.

The interlayer spacing (*d*) was calculated using Eq. (1) (Bragg's equation) and

$$n\lambda = d\sin\theta, \quad (1)$$

where λ and θ are the wavelength of X-ray and Bragg's angle, respectively.

The *d* spacing in GO was 0.8 nm which reduced to 0.38 nm in rGO. This shows that GO is successfully reduced to rGO. This occurs because, on reduction, the water molecules and the oxygen functionalities are removed, which is shown by the FTIR analysis. The reason for the decrease of *d* value is the breaking of hydrogen bonding between the water molecules and oxygen functional groups of GO [34]. As the amount of aniline was increased, the intensity of peaks for PANI increased and that for Cu₂O decreased.

The Raman spectra of CRP composites in the range 100 to 3500 cm⁻¹ are displayed in Fig. 2a. The formation of Cu₂O was shown by the peaks located at 260.49 and 611.01 cm⁻¹ [41]. The peaks at 817.44 and 1079.15 cm⁻¹ arise due to the benzene ring's deformation and the stretching vibrations for the C–H bonds in the benzenoid ring, respectively [42]. Here, the D and G bands for PANI and rGO cannot be differentiated because both give similar Raman features as both contain similar carbon skeletons. This is because the p orbitals of rGO and PANI overlap and form an integrated structure [43, 44]. So, to further interpret the Raman spectra and gain more understanding, the D and G bands were deconvoluted into four Gaussian peaks (Fig. 2b). The peaks centered at

Fig. 1 **a** XRD patterns of GO, rGO, and PANI. **b** XRD patterns of CRP0.5, CRP1, and CRP1.5

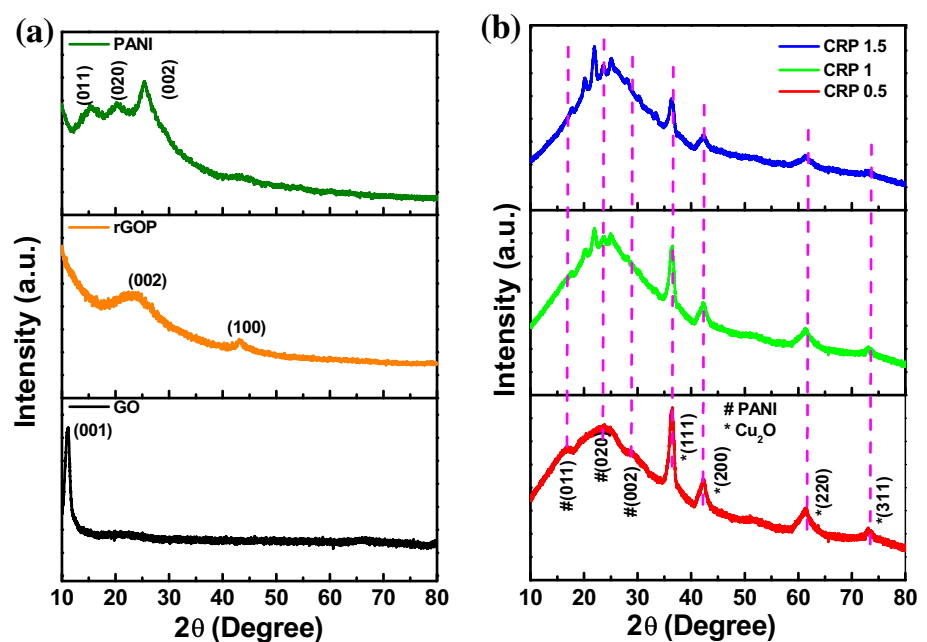
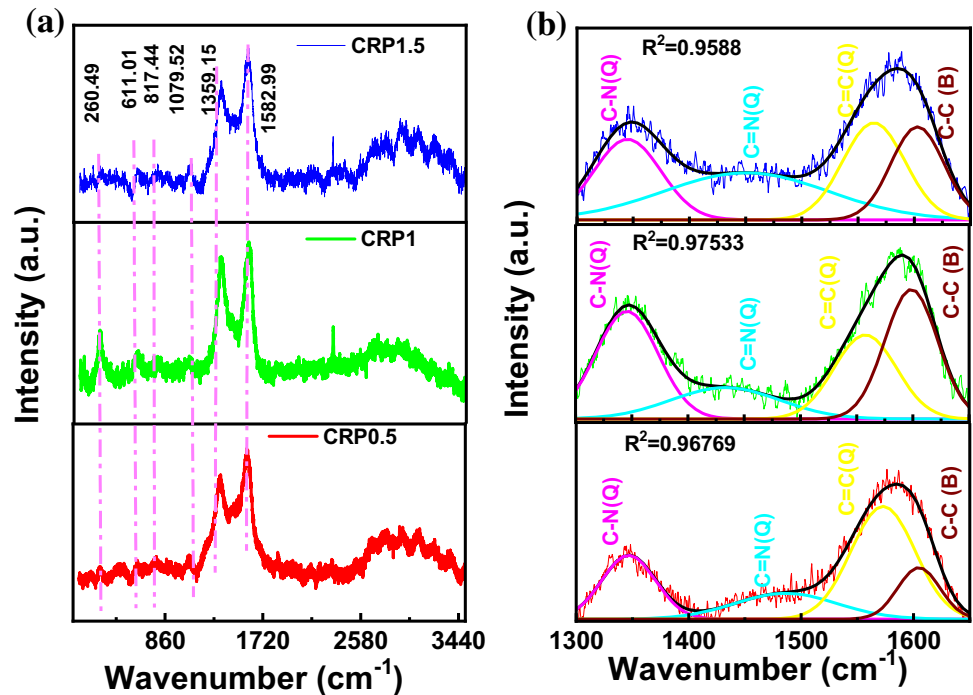


Fig. 2 **a** Raman spectra of CRP0.5, CRP1, and CRP1.5 in the range 100 to 3500 cm^{-1} . **b** Deconvoluted D and G bands of CRP0.5, CRP1, and CRP1.5



$\sim 1345.7, 1450.5, 1557.7,$ and 1598.6 cm^{-1} correspond to C–N, C=N, C=C, and C–C stretching vibrations in the quinoid and benzenoid ring, respectively [42]. The intensity of the C=N peak is observed to be less as the amount of $\text{Cu}_2\text{O}/\text{rGO}$ is increased in the composite. The broad peak in the range 2500 to 3500 cm^{-1} is for the 2D band of rGO [45].

3.3 Optical studies

Fig. S2a presents the UV–visible spectra for GO, rGO, and PANI. The UV–visible spectrum of GO consists of a peak at 248.7 nm, which is the resultant of $\pi \rightarrow \pi^*$ transitions. Another peak at 317.2 nm is for the $n \rightarrow \pi^*$ electronic transition due to the presence of non-bonding electrons in carbonyl groups (C=O) [46]. However, the latter peak disappeared in the case of rGO, and the former peak shows a bathochromic shift to 301.2 nm, suggesting an increase in the number of C=C bonds and a decrease in that of C=O bonds, respectively [47]. The peak at 266.5 nm in the spectrum of PANI is for the $\pi \rightarrow \pi^*$ in the aromatic ring [48]. The absorbance peak at 382.5 nm corresponds to the $n \rightarrow \pi^*$ transition in the quinoid ring. The broadband at above 600 nm is assigned to polaron $\rightarrow \pi^*$ transition [49]. As the composite is synthesized, the following changes are observed in their spectra (Fig. S2b):

- (i) The peaks for $\pi \rightarrow \pi^*$ and $n \rightarrow \pi^*$ show a bathochromic shift because as rGO and PANI are integrated, both the sp^2 carbons and the nonbonding electrons are increased. The FTIR analysis showed the presence of C=C, C=O, and C = N bonds which are responsible for these transitions.
- (ii) There is an increase in the intensity and sharpness of the peak for polaron $\rightarrow \pi^*$ transition in CRP samples and is maximum for CRP1.5. This is because as the amount of polyaniline increases, the number of polarons also enhances, which causes a greater probability for electronic excitation (ϵ).
- (iii) Furthermore, a similar increase is observed for peaks related to $\pi \rightarrow \pi^*$. This is because the incorporation of PANI in $\text{Cu}_2\text{O}/\text{rGO}$ increases the number of C=C bonds. So, the probability of electronic transition from π to π^* orbital increases leading to the observed increase in intensity.

The bandgap energy was calculated using Eq. (2):

$$\alpha h\nu = B(h\nu - E_g)^n, \tag{2}$$

where $B, h, \alpha,$ and ν refer to the proportionality constant, Planck constant, absorption coefficient, and frequency of the light. Here, $n = 2$ as the as-

synthesized samples possess a direct bandgap. The optical band gap energies were obtained by extrapolating the linear portion of the curve to the X-axis (Fig. S2c). The obtained values of bandgap energies for GO, rGO, PANI, CRP0.5, CRP1, and CRP1.5 were 2.99, 1.72, 2.75, 2.39, 2.32, and 2.29 eV, respectively. The bandgaps of GO, rGO, and PANI are comparable to the earlier reported values in the literature [50–52].

3.4 Morphological studies

The SEM images of both CRP0.5 and CRP1.5 show the presence of spherical structures distributed over the sample (Fig. 3). These spheres are composed of Cu₂O nanoparticles wrapped with rGO–PANI sheets. In addition to that, some rGO–PANI lumps can be seen in the background. This confirms the complete utilization of rGO–PANI sheets by Cu₂O nanoparticles.

Moreover, it was observed that in the case of CRP0.5, small-sized spherical particles are densely distributed over the rGO sheet (Fig. 3a and b). In this case, the concentration of PANI was taken low, due to which complete wrapping of PANI for all the available Cu₂O nanoparticles was not possible. While in the case of CRP1.5, comparatively more significant-sized spheres were produced as the concentration of PANI was increased (Fig. 3c and d). Hence, a large number of Cu₂O nanoparticles were covered with the rGO–PANI sheets. The schematic for the preparation of the CRP composite is shown in Fig. S3. The encapsulation of Cu₂O nanoparticles by rGO and PANI was studied separately by Ganesh babu et al. [53] and Singh et al. [54].

3.5 Elemental analysis

The bonding nature and elemental composition of the CRP composites were further studied by XPS analysis. The wide-scan spectrum for CRP0.5 and CRP1.5 is presented in Fig. S4. C, N, and O in the composites are confirmed by the peaks centered at ~ 282.9, 398.2, and 530.6, respectively [55]. However, the peak for Cu was not observed in XPS. This reason may be the low content of Cu. The other reason may be, the Cu₂O formed were present in the inner sites of the material and not on the surface. Since XPS is a surface phenomenon and analyzes only the top 5 to 10 atomic layers, it may not be able to detect Cu.

The C1s core orbital was deconvoluted into three peaks using Gaussian fitting (Fig. 4a). The peaks corresponding to C=C, C–N, and C=O are observed at 284.88, 286.28, and 288.01 eV for CRP0.5 and 284.59, 285.88, and 288.23 eV for CRP1.5, respectively. Comparing the C=C to C–N bond ratio for both CRP0.5 and CRP1.5, we observed that the intensity ratio reduces in the case of CRP1.5, corresponding to the increased number of C–N bonds in the PANI–rGO matrix.

Similarly, N1s core orbital was deconvoluted into two Gaussian peaks (Fig. 4b). The peaks corresponding to N–C and N–N bonds were at 399.71 and 400.89 eV for CRP0.5 and 399.53 and 400.98 eV for CRP1.5, respectively. The high-intensity ratio of the N–C and N–N peaks corresponds to a high doping level of PANI in CRP1.5. Further, the spectrum for O1s core orbital was deconvoluted into three Gaussian peaks (Fig. 4c). For both the samples, the O1s peaks show similar results. The peaks corresponding to O–C–C, O–C=C, and O–N–C are centered at 531.14, 532.66, and 533.60 eV for CRP0.5 and 531.00, 532.57, and 534.18 eV for CRP1.5, respectively [22]. From XPS analysis, it is evident that the composites consist of the elements C, O, and N. However, it could not detect Cu, the probable reasons for which are mentioned above. Moreover, the bonding and vibrations, structural analysis, and optical studies show the successful formation of CRP composites.

3.6 Electrochemical studies

Figure 5a–c represents the CV curves of the CRP composites recorded in the range 0 to 0.8 V at scan rates of 1, 5, 10, 50, and 100 mV/s. The measurement was done in a three-electrode cell system using 1 M H₂SO₄ as the electrolyte. The CV curves possess distorted rectangular shapes with oxidation and reduction peaks suggesting the redox reactions occurring due to the presence of rGO, PANI, and Cu₂O in the composite. All the CV profiles show electrochemical double-layer capacitance (EDLC) along with pseudocapacitance behavior. With the increase in the scan rates, it was observed that the oxidation peaks shifted toward positive potential, and reduction peaks shifted toward negative value. The shift in the peaks confirms the pseudocapacitance nature of the CRP composites. The current response for all the composites increases with the scan rate because the kinetics of the redox reaction

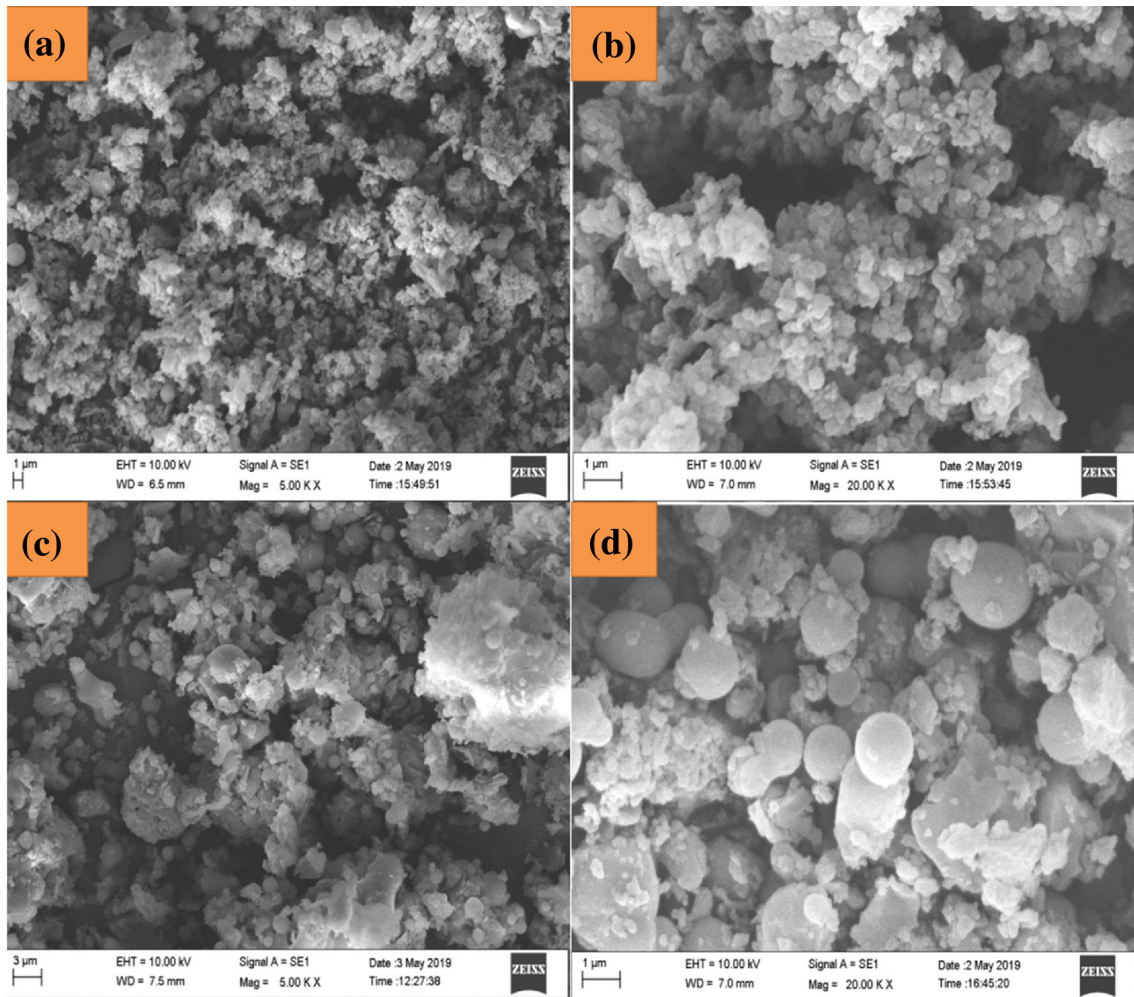


Fig. 3 SEM images of **a** CRP0.5 and **c** CRP1.5 composites. Magnified SEM images of **b** CRP0.5 and **d** CRP1.5

and the rate at which the ions and electrons respond is faster at high scan rates [56].

Further, it is observed that the area under the curve increases, but C_{sp} decreases at higher scan rates. Figure 5d shows the variation of C_{sp} with the scan rate. The C_{sp} values are lower at high scan rates because the diffusion of electrolytes into the electrode material is low. However, as the scan rate decreases, the degree of diffusion increases, letting the electrolyte interact more with the electrode material. The electrolyte will get enough time to interact with the interstitial sites of the electrode material, which can be used for charge storage [57]. Hence, the C_{sp} value at 1 mV/s was highest for all composites. The C_{sp} value was calculated using Eq. (3):

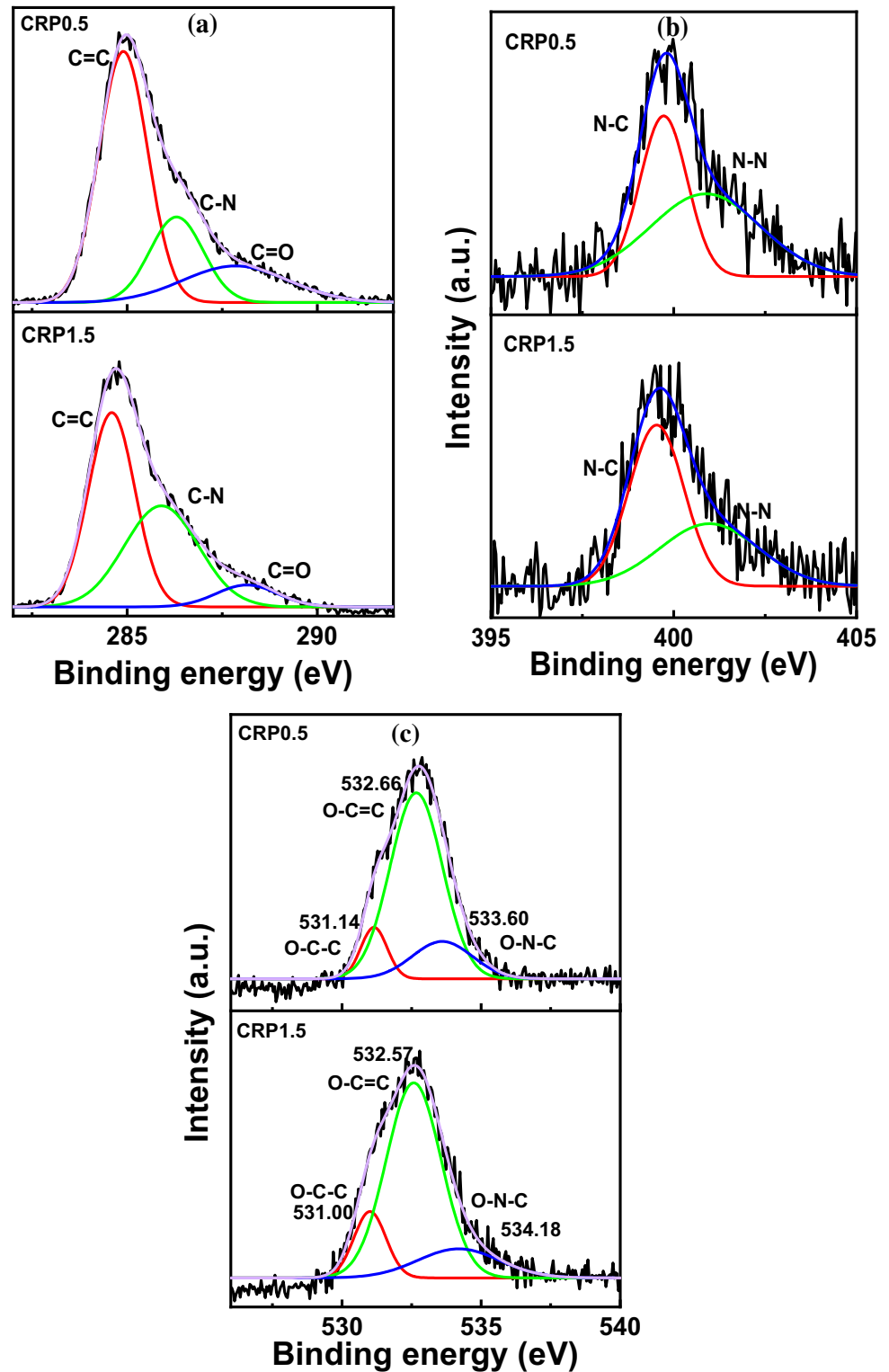
$$C_{sp} = \frac{\int IdV}{S\Delta Vm} \tag{3}$$

Here, $\int IdV$ = Integrated area under the CV curve, S = scan rate (mV/s), m = the mass of active material (mg), and ΔV = potential window (V).

The calculated values of C_{sp} for all CRP composites are inserted in Table 1. We found that the C_{sp} value was highest for CRP1.5 at all scan rates from the obtained data. The C_{sp} value increased as the amount of PANI was increased in the composites. This may be due to the increase in redox sites and conductivity of the composite as the content of PANI was increased [58].

To further study the behavior of the CRP composites as supercapacitor electrode material, GCD was recorded in the potential range 0 to 0.8 at current densities 1A/g, 0.5A/g, 0.3 A/g, and 0.1 A/g. The GCD curves for the CRP composites are presented in Fig. 6a–c. The C_{sp} values were calculated using Eq. 4:

Fig. 4 Deconvoluted XPS spectra of core orbital **a** C1s, **b** N1s, and **c** O1s for CRP0.5 and CRP1.5



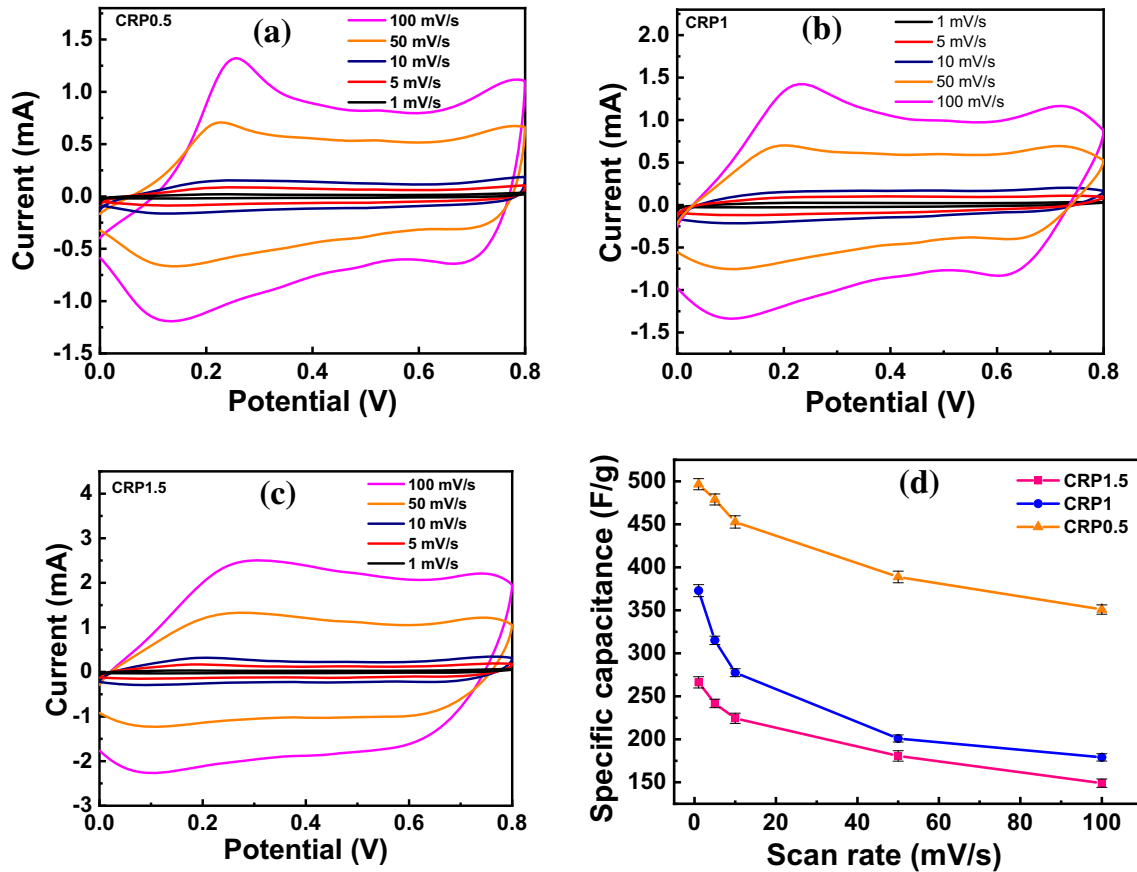


Fig. 5 CV profiles for **a** CRP0.5, **b** CRP1, and **c** CRP1.5 composites. **d** Scan rate versus specific capacitance for CRP composites

Table 1 Specific capacitance values obtained from CV and GCD curves

Sample codes	@Scan rates (Vs ⁻¹)					@Current densities (Ag ⁻¹)			
	1	5	10	50	100	0.1	0.3	0.5	1
CRP0.5	266.19	241.70	224.40	180.63	148.99	127.59	118.97	114.81	112.85
CRP1	372.84	315.05	277.46	200.94	179.01	193.07	171.51	156.85	118.70
CRP1.5	496.61	478.94	452.76	388.79	350.94	221.99	205.84	191.73	162.88

$$C_{sp} = \frac{I\Delta t}{m\Delta V} \tag{4}$$

The calculated values of C_{sp} are inserted in Table 1. CRP0.5, CRP1, and CRP1.5 show C_{sp} values of 127.59, 193.07, and 221.99 F/g at a current density of 0.1 A/g. From GCD, also CRP1.5 shows the highest C_{sp} value supporting the results obtained from CV analysis. Figure 6d shows the plot of C_{sp} versus current density. The C_{sp} values decrease with an increase in current density because of the poor interaction between the electrode and electrolyte due to time constraints.

The EIS is vital for studying the interactions and kinetics of the reaction at the electrode/electrolyte surface. This study was done in the frequency range of 0.1 to 10⁶ Hz and 0.3 V for all the composites. From the experiment for EIS, the Nyquist plot was obtained, which is a plot of real *vs* imaginary impedance (Fig. 7a). The inset in Fig. 7a is the circuit diagram for the Nyquist plot, which was obtained by fitting the curves using ZView software. Here, R_e , R_{CT} , C_{dl} , and W refer to electrolytic resistance, charge transfer resistance, double-layer capacitance, and Warburg impedance, respectively.

The values thus obtained after fitting the curves such as R_e , R_{CT} , Chi-square, C_{dl} , and W are given in

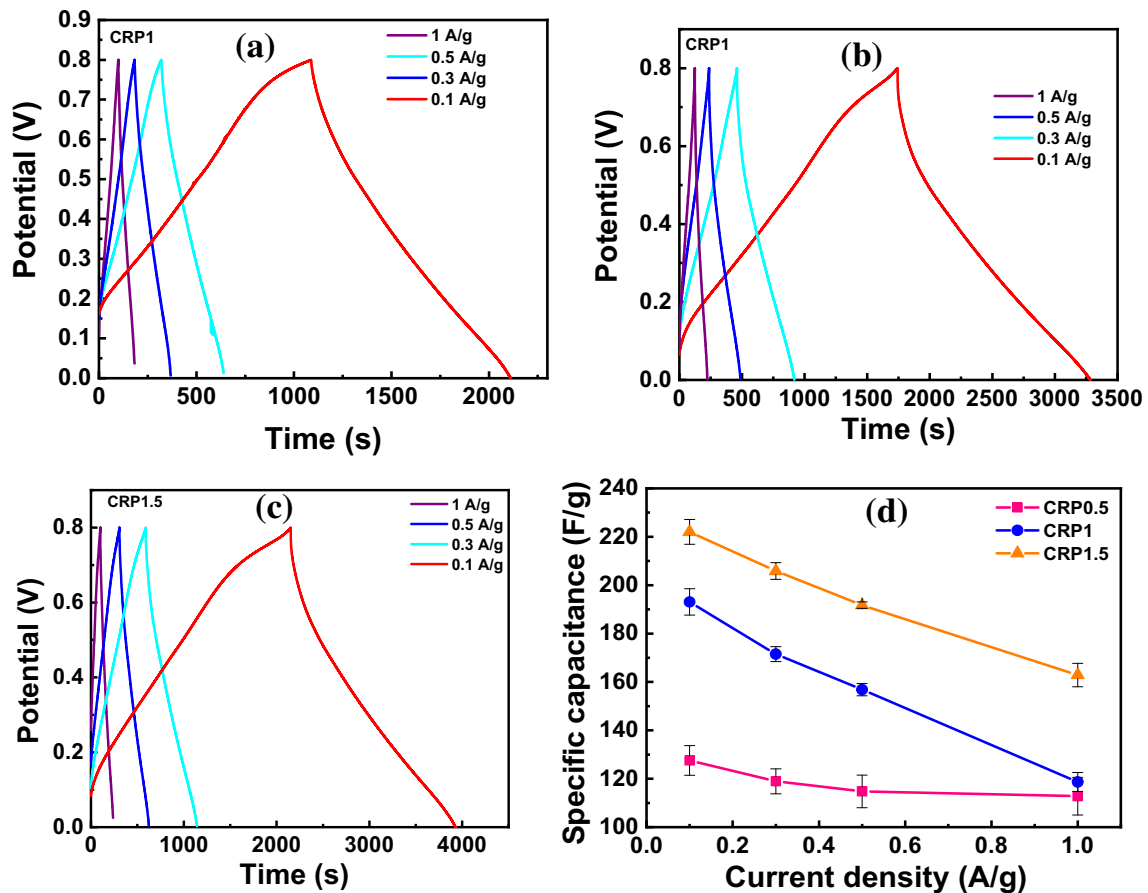


Fig. 6 Galvanostatic charge–discharge curves for **a** CRP0.5, **b** CRP1, and **c** CRP1.5. **d** Specific capacitance values of the composites at different current densities

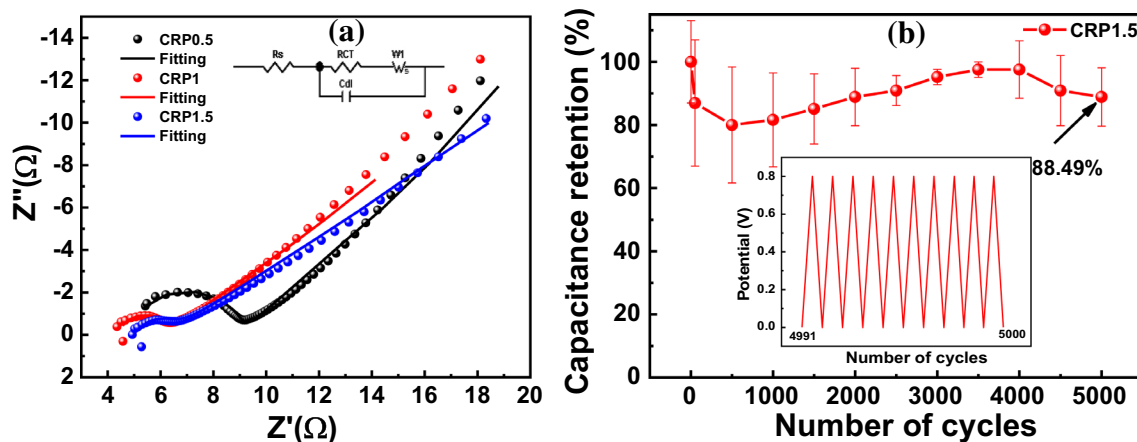


Fig. 7 **a** Nyquist plot of CRP0.5, CRP1, and CRP1 fitted using ZView software. **b** Cycle life at a current density of 1 A/g

Table 2. The R_{CT} value is observed to be in the order CRP0.5 > CRP1 > CRP1.5. CRP1.5 has the lowest R_{CT} value depicting the lowest charge transfer resistance between the electrode and the electrolyte. The C_{dl} and W value obtained from the Nyquist plot's fitting is

also highest for CRP1.5. This also explains the higher value of C_{sp} for CRP1.5, which is observed in CV and GCD analysis.

The efficiency of the supercapacitor depends significantly on its cycle life. Since the CRP1.5 shows the

Table 2 Values obtained from Nyquist plot after fitting with Z-view software

Sample codes	Chi-square	R_e		R_{CT}		C_{dl}		Total W Value (Ω)
		Value (Ω)	Error (%)	Value (Ω)	Error (%)	Value $\times 10^{-7}$ (F/cm ²)	Error (%)	
CRP0.5	0.0009	4.95	1.34	4.03	1.75	1.49	4.13	41.17
CRP1	0.0009	4.45	0.95	1.74	2.92	4.99	6.24	31.98
CRP1.5	0.0014	5.17	1.06	1.17	6.46	8.37	11.37	43.36

highest value of C_{sp} , it was subjected to 5000 cycles of charge and discharge (Fig. 7b). After 5000 cycles, the material shows an excellent capacitance retention value of 88.49%. An initial reduction in capacitance retention is observed, which may be because the system requires time to stabilize. Initially, the reduction may also occur due to the time required by the electrolyte to seep into the electrode material [59]. After 500 cycles, the system becomes stable, and the capacitance increases steadily up to 4000 cycles. The capacitance increases as the CRP is activated and provides accessible sites for the electrolyte to interact. rGO prevents PANI deformation, and PANI, in turn, acts as a protective layer to rGO and CuO [60]. The capacitance decreases slowly after 4000 cycles which may be due to the gradual degradation of the sample.

4 Conclusion

An eco-friendly, inexpensive, and facile method was used to synthesize CRP composites. A simple reflux system is used for the synthesis process using *Citrus maxima* juice as the reducing agent. The use of a bio-reducing agent overcomes the drawbacks of toxic chemical agents. This study contributes to the search for an eco-friendly and efficient method for the synthesis of CRP composites. This material showed a high C_{sp} value of 496.61 F/g with excellent cycling stability. The results of this study showed CRP to be an excellent electrode material for supercapacitors applications.

Acknowledgements

Ms. Sadhna Rai is obliged to UGC-DAE-CSR, Indore (Project Ref: CSR-IC-MSR-07/CRS-215/2017-18/1296) for Grant-in-Aid for Junior Research Fellowship. The authors thank the Sophisticated Analytical

Instrumentation Facility, IIT Bombay and Institute Instrumentation Centre, IIT Roorkee for their help in acquiring Raman spectroscopy and XPS data, respectively.

Declarations

Conflict of interest On behalf of all authors, the corresponding author states that there is no conflict of interest.

Supplementary Information The online version contains supplementary material available at <http://doi.org/10.1007/s10854-021-07175-9>.

References

1. P. Simon, Y. Gogotsi, B. Dunn, *Science* **343**, 1210 (2014)
2. M.A.A. Mohd Abdah, N.H.N. Azman, S. Kulandaivalu, Y. Sulaiman, *Mater. Des.* **186**, 108199 (2020)
3. S. Tajik, D.P. Dubal, P. Gomez-Romero, A. Yadegari, A. Rashidi, B. Nasernejad, A.M. Asiri, *Int. J. Hydrogen Energy* **42**, 12384 (2017)
4. Y. Wang, L. Zhang, H. Hou, W. Xu, G. Duan, S. He, K. Liu, S. Jiang, *J. Mater. Sci.* **56**, 173 (2021)
5. C. Zhao, X. Jia, K. Shu, C. Yu, G.G. Wallace, C. Wang, *J. Mater. Chem. A* **8**, 4677 (2020)
6. Q. Meng, K. Cai, Y. Chen, L. Chen, *Nano Energy* **36**, 268 (2017)
7. P.S. Murphin Kumar, H.H. Kyaw, M.T.Z. Myint, L. Al-Haj, A.H. Al-Muhtaseb, M. Al-Abri, V. Thanigaivel, V.K. Ponnusamy, *Int. J. Energy Res.* **44**, 10682 (2020)
8. B. Ameri, S.S.H. Davarani, R. Roshani, H.R. Moazami, A. Tadjarodi, *J. Alloys Compd.* **695**, 114 (2017)
9. A.K. Mishra, A.K. Nayak, A.K. Das, D. Pradhan, *J. Phys. Chem. C* **122**, 11249 (2018)
10. X. Dong, K. Wang, C. Zhao, X. Qian, S. Chen, Z. Li, H. Liu, S. Dou, *J. Alloys Compd.* **586**, 745 (2014)

11. D.P. Dubal, D.S. Dhawale, R.R. Salunkhe, V.S. Jamdade, C.D. Lokhande, *J. Alloys Compd.* **492**, 26 (2010)
12. G.A. Snook, P. Kao, A.S. Best, *J. Power Sources* **196**, 1 (2011)
13. K.S. Kim, Y. Zhao, H. Jang, S.Y. Lee, J.M. Kim, K.S. Kim, J.-H. Ahn, P. Kim, J.-Y. Choi, B.H. Hong, *Nature* **457**, 706 (2009)
14. C. Lee, X. Wei, J.W. Kysar, J. Hone, *Science (80-.)* **321**, 385 (2008)
15. S. Mahata, A. Sahu, P. Shukla, A. Rai, M. Singh, V.K. Rai, *New J. Chem.* **42**, 19945 (2018)
16. C. Li, Z. Zhuang, X. Jin, Z. Chen, *Appl. Surf. Sci.* **422**, 469 (2017)
17. S. Kumar, D. Bhorolua, A.K. Ojha, A. Kumar, *Adv. Mater. Lett.* **10**, 58 (2019)
18. M.Z. Ansari, R. Johari, W.A. Siddiqi, *Mater. Res. Express* **6**, 055027 (2019)
19. P. Haldar, S. Biswas, V. Sharma, A. Chowdhury, A. Chandra, *Appl. Surf. Sci.* **491**, 171 (2019)
20. S. Zhu, M. Wu, M.-H. Ge, H. Zhang, S.-K. Li, C.-H. Li, *J. Power Sources* **306**, 593 (2016)
21. A. Gupta, S. Sardana, J. Dalal, S. Lather, A.S. Maan, R. Tripathi, R. Punia, K. Singh, A. Ohlan, *A.C.S. Appl. Energy Mater.* **3**, 6434 (2020)
22. S. Sinha, N.A. Devi, S. Nongthombam, R. Bhujel, S. Rai, G. Sarkar, B.P. Swain, *Diam. Relat. Mater.* **107**, 107885 (2020)
23. K.A. Ali, R. Yao, W. Wu, M.M.I. Masum, J. Luo, Y. Wang, Y. Zhang, Q. An, G. Sun, B. Li, *Mater. Res. Express* **7**, 015097 (2020)
24. M.Y. Ali, N.-E.N. Rumpa, S. Paul, M.S. Hossen, E.M. Tanvir, T. Hossan, M. Saha, N. Alam, N. Karim, M.I. Khalil, S.H. Gan, *J. Toxicol.* **2019**, 1 (2019)
25. G. Xu, D. Liu, J. Chen, X. Ye, Y. Ma, J. Shi, *Food Chem.* **106**, 545 (2008)
26. S. Kumar, A.K. Pandey, *Sci. World J.* **2013**, 1 (2013)
27. D.C. Marcano, D.V. Kosynkin, J.M. Berlin, A. Sinitskii, Z. Sun, A. Slesarev, L.B. Alemany, W. Lu, J.M. Tour, *ACS Nano* **4**, 4806 (2010)
28. B.D. Ossoinon, D. Bélanger, *RSC Adv.* **7**, 27224 (2017)
29. D. He, Z. Peng, W. Gong, Y. Luo, P. Zhao, L. Kong, *RSC Adv.* **5**, 11966 (2015)
30. H. Zhang, D. Hines, D.L. Akins, *Dalt. Trans.* **43**, 2670 (2014)
31. Z. Durmus, B.Z. Kurt, A. Durmus, *ChemistrySelect* **4**, 271 (2019)
32. P. Benjwal, M. Kumar, P. Chamoli, K.K. Kar, *RSC Adv.* **5**, 73249 (2015)
33. J.R.N. Santos, D.S.S. Viégas, I.C.B. Alves, A.D. Rabelo, W.M. Costa, E.P. Marques, L. Zhang, J. Zhang, A.L.B. Marques, *Electrocatalysis* **10**, 560–572 (2019)
34. Y. Zhang, J. Liu, Y. Zhang, J. Liu, Y. Duan, *RSC Adv.* **7**, 54031 (2017)
35. B. Butoi, A. Groza, P. Dinca, A. Balan, V. Barna, *Polymers (Basel)* **9**, 732 (2017)
36. J. Luo, Q. Ma, H. Gu, Y. Zheng, X. Liu, *Electrochim. Acta* **173**, 184 (2015)
37. K. Karthik, N. Victor Jaya, M. Kanagaraj, S. Arumugam, *Solid State Commun.* **151**, 564 (2011)
38. H.R. Naderi, A. Sobhani-Nasab, M. Rahimi-Nasrabadi, M.R. Ganjali, *Appl. Surf. Sci.* **423**, 1025 (2017)
39. P. Martis, A. Fonseca, Z. Mekhalif, J. Delhalle, *J. Nanoparticle Res.* **12**, 439 (2010)
40. K.R. Reddy, B.C. Sin, C.H. Yoo, W. Park, K.S. Ryu, J.-S. Lee, D. Sohn, Y. Lee, *Scr. Mater.* **58**, 1010 (2008)
41. A. Chakravarty, K. Bhowmik, A. Mukherjee, G. De, *Langmuir* **31**, 5210 (2015)
42. M. Trchová, Z. Morávková, M. Bláha, J. Stejskal, *Electrochim. Acta* **122**, 28 (2014)
43. G. Zhang, X. Xiao, B. Li, P. Gu, H. Xue, H. Pang, *J. Mater. Chem. A* **5**, 8155 (2017)
44. Y. Tian, Y. Wang, Y. Wang, L. Ma, X. Gao, *Mater. Res. Express* **6**, 105614 (2019)
45. S. Rai, R. Bhujel, J. Biswas, B.P. Swain, *Ceram. Int.* **45**, 14136 (2019)
46. C.H. Manoratne, S.R.D. Rosa, I.R.M. Kottegoda, *Mater. Sci. Res. India* **14**, 19 (2017)
47. Abid, P. Sehrawat, S.S. Islam, P. Mishra, and S. Ahmad, *Sci. Rep.* **8**, 3537 (2018).
48. S. Saha, N. Chaudhary, A. Kumar, M. Khanuja, S.N. Appl, *Sci.* **2**, 1115 (2020)
49. V.A. Mooss, A.A. Athawale, *J. Polym. Sci. Part A Polym. Chem.* **54**, 3778 (2016)
50. H.-C. Hsu, I. Shown, H.-Y. Wei, Y.-C. Chang, H.-Y. Du, Y.-G. Lin, C.-A. Tseng, C.-H. Wang, L.-C. Chen, Y.-C. Lin, K.-H. Chen, *Nanoscale* **5**, 262 (2013)
51. M.A. Velasco-Soto, S.A. Pérez-García, J. Alvarez-Quintana, Y. Cao, L. Nyborg, L. Licea-Jiménez, *Carbon N. Y.* **93**, 967 (2015)
52. M. Shah, N. Khan, Z. Imran, M. Khan, A. Khattak, A. Khan, N. Ullah, *Mater. Res. Express* **7**, 015314 (2019)
53. S. Ganesh Babu, R. Vinoth, P. Surya Narayana, D. Bahne-mann, B. Neppolian, *APL Mater.* **3**, 104415 (2015)
54. P. Singh, S.K. Shukla, *Surf. Interfaces* **18**, 100410 (2020)
55. A. Moysowicz, G. Gryglewicz, *Compos. Part B Eng.* **159**, 4 (2019)
56. A. Aljaafari, N. Parveen, F. Ahmad, M.W. Alam, S.A. Ansari, *Sci. Rep.* **9**, 9140 (2019)
57. R. Bhujel, S. Rai, K. Baruah, U. Deka, J. Biswas, B.P. Swain, *J. Sci. Rep.* **9**, 1–14 (2019)
58. A. Viswanathan, A.N. Shetty, *Electrochim. Acta* **289**, 204 (2018)

59. Y. Tan, Z. Jia, J. Sun, Y. Wang, Z. Cui, X. Guo, J. Mater. Chem. A **5**, 24139 (2017)
60. P. Xiong, H. Huang, X. Wang, J. Power Sources **245**, 937 (2014)

Publisher's Note Springer Nature remains neutral with regard to jurisdictional claims in published maps and institutional affiliations.